Rheology of a dilute ferrofluid droplet suspension in shear flow: Viscosity and normal stress differences

Ishida, Shunichi

Matsunaga, Daiki

(Citation)
Physical Review Fluids,5(12):123603-123603

(Issue Date)
2020-12-15

(Resource Type)
journal article

(Version)
Version of Record

Rheology of a dilute ferrofluid droplet suspension in shear flow: Viscosity and normal stress differences

Shunichi Ishida*
Graduate School of Engineering, Kobe University, Rokkodai 6578501, Japan

Daiki Matsunaga†
Graduate School of Engineering Science, Osaka University, Toyonaka 5608531, Japan

(Received 9 May 2020; accepted 24 November 2020; published 15 December 2020)

We report the rheology of a dilute ferrofluid droplet suspension under simple shear flow, using the three-dimensional lattice-Boltzmann simulation and the phase-field model. In our simulation, we utilize 12M computational grids to fully resolve the droplet deformation, and GPU parallelization is used to speed up the computation. The droplet deformation is determined by both the background shear flow and the external magnetic field effects. The ferrofluid droplet has a character to elongate in the direction of the external field, and a uniform static magnetic field is applied to the system to control the droplet shape. By changing the external field strength and direction, we found that the suspension rheologies can be drastically modified. The viscosity increase (decrease) with the external field when the external field is applied to the velocity gradient direction (velocity direction). Just by imposing the external magnetic field, the specific viscosity becomes $12 \sim 620\%$ of the viscosity under no external magnetic field. The magnetic force is also practical to control the normal stresses, since the normal stress in ith direction decreases when the magnetic field is applied to the ith direction. Therefore, in order to increase (decrease) the first normal stress difference N_1, the external magnetic field should be applied to the velocity direction (velocity gradient direction). To increase (decrease) the second normal stress difference N_2, the external magnetic field should be applied to the velocity gradient direction (vorticity direction). By applying the magnetic field, we also show that the normal stresses N_1, N_2 even show opposite sign from the normal droplet solution ($N_1 > 0$, $N_2 < 0$) under small-Reynolds-number conditions. Our work suggests that the ferrofluid droplet would be a practical complex fluid to control the suspension properties, just by changing the external magnetic field strength and directions.

DOI: 10.1103/PhysRevFluids.5.123603

I. INTRODUCTION

Magnetic force allows to control and micro-sized object in viscous fluids. Using magnetic colloids, there have been many applications suggested [1,2] in recent years such as magnetic swimmers [3–5], magnetic pump and cilia [6], magnetic mixers [7,8], and particle sorting and segregations [9–14]. A ferromagnetic colloid feels torque by applying a uniform magnetic field and aligned itself to the direction of the magnetic field. When a uniform, static magnetic field is applied to a ferrofluid droplet, the droplet elongates in the direction of the external field [15–18]. In recent years, there are several interesting works [19] that utilize this character of the ferrofluid

*ishida@mech.kobe-u.ac.jp
†daiki.matsunaga@me.es.osaka-u.ac.jp

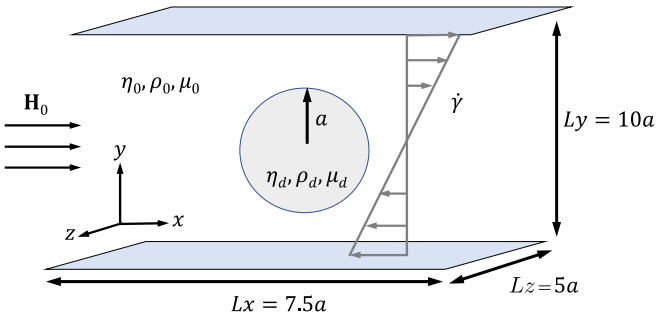

FIG. 1. A schematic illustration of the problem statement.

droplet to control the fluid properties. Wang and his coauthors [13,14] reported that the destination of the ferrofluid droplet inside a microfluidic channel can be controlled by the external magnetic field, using both two-dimensional (2D) simulation [13] and experiments [14]. When a droplet is flowing inside a small channel under the Poiseuille flow, the droplet usually migrates toward the channel center because of its deformation and image stresslet effect [11,12,20]; the particles show cross-streamline migration due to the hydrodynamic interaction with the channel wall. Controlling the elongational direction of the droplet by the external magnetic field, they showed that the droplet position can be controlled not only to the channel center but also toward the channel wall.

Cunha *et al.* [21,22] showed that the ferrofluid droplet can be utilized to control the suspension rheology. In their works, they evaluated the viscosity [21] and the normal stress differences [22] of the droplet suspension that is located between two parallel plates using 2D simulation. Depending on the elongational direction of the droplet, the viscosity changes drastically: The suspension viscosity increases by five times when the external field is applied perpendicular to the shear velocity, while it decreases to half when the magnetic field is applied parallel to the shear flow. They also presented for the first time how the droplet breaks up because of the external magnetic field.

Compared to the understanding of the droplet deformations, the rheological properties of this solution are not well known. In this work, our motivation is to systematically investigate the rheology of dilute solutions of a ferrofluid droplet under the shear flow, using three-dimensional lattice-Boltzmann simulations. We consider a ferrofluid droplet that is placed between two parallel plates and evaluate the properties of the solution under both effects of the background shear flow and the external magnetic field. In order to fully resolve the droplet deformation, 12M computational grids are utilized in our 3D simulation. Note that most of the simulations in the previous works were done in 2D systems [13,21–23] because of the heavy computational load, except an advanced work of the 3D simulation [24]. In this work, we first evaluate how the droplet elongations and deformations are modified due to the external magnetic field. Second, we report how the suspension rheologies, such as the specific viscosity and the normal stress differences N_1 and N_2, are revised due to the external magnetic field. Controlling the magnetic field direction and strength, we show that the viscosity can be controlled and the normal stress differences can be opposite from the normal droplet solution ($N_1 > 0, N_2 < 0$) [25] under the small-Reynolds-number conditions.

II. PROBLEM STATEMENT AND METHOD

A. Problem statement

Figure 1 shows the problem statement of our present work. Consider a ferrofluid droplet with a radius a located in between two parallel plates which has a width L_y, and the domain size is $L_x \times L_y \times L_z = 7.5a \times 5.0a \times 10.0a$. A simple shear flow with a shear rate $\dot{\gamma}$ is generated by moving the top wall with a velocity $\boldsymbol{u} = (\dot{\gamma} L_y/2, 0, 0)$ and the bottom with a velocity $\boldsymbol{u} = (-\dot{\gamma} L_y/2, 0, 0)$. The periodic boundary condition is applied to both x and z directions. The droplet

consists of a fluid with the viscosity η_d, density ρ_d, magnetic permeability μ_d, while the surrounding fluid has the viscosity η_0, density ρ_0, and magnetic permeability μ_0. In this paper, we do not consider the viscosity and density difference between two fluids, and the permeability ratio is fixed to 2 (i.e., $\eta_d/\eta_0 = 1$, $\rho_d/\rho_0 = 1$, and $\mu_d/\mu_0 = 2$). Note that μ_0 is assumed to be equal to the vacuum permeability.

In this paper, we analyze the droplet deformation under both effects of the simple shear flow and a uniform external magnetic field $\boldsymbol{H}_0$.

B. Governing equations

1. Two-phase flow dynamics

The two-phase flow hydrodynamics is solved by using incompressible Navier-Stokes equation with additional forcing term:

$$\nabla \cdot \boldsymbol{u} = 0, \tag{1}$$

$$\rho\left(\frac{\partial \boldsymbol{u}}{\partial t} + \boldsymbol{u} \cdot \nabla \boldsymbol{u}\right) = -\nabla p + \eta \nabla^2 \boldsymbol{u} + \boldsymbol{f}_s + \boldsymbol{f}_m, \tag{2}$$

where $\boldsymbol{u}$ is the velocity field, p is the pressure, ρ is the density, η is the viscosity, $\boldsymbol{f}_s$ is the surface tension force, and $\boldsymbol{f}_m$ is the magnetic force. To capture the interface dynamics, we solve the conservative phase-field equation [26],

$$\frac{\partial \phi}{\partial t} + \boldsymbol{u} \cdot \nabla \phi = \nabla \cdot \left\{ M\left[\nabla \phi - \frac{4}{\xi}\phi(1-\phi)\boldsymbol{n}\right]\right\}, \tag{3}$$

where $\phi \in [0, 1]$ is the phase function, ξ is the interface thickness, M is the mobility, and $\boldsymbol{n} = \nabla\phi/|\nabla\phi|$ is the unit normal vector on the interface that points outward (surrounding fluids). The surface tension force $\boldsymbol{f}_s$ is calculated by using the continuum surface force model [27],

$$\boldsymbol{f}_s = \sigma \kappa \nabla \phi, \tag{4}$$

where σ is the surface tension and κ is the curvature defined as

$$\kappa = -\nabla \cdot \boldsymbol{n}. \tag{5}$$

2. Magnetic field

The magnetic flux density $\boldsymbol{B}$ can be described using the magnetization $\boldsymbol{M}$ and the magnetic field strength $\boldsymbol{H}$ as

$$\boldsymbol{B} = \mu_0(\boldsymbol{H} + \boldsymbol{M}). \tag{6}$$

By assuming that the ferrofluid is superparamagnetic $\boldsymbol{M} = \chi \boldsymbol{H}$, Eq. (6) is modified as

$$\boldsymbol{B} = \mu_0(1+\chi)\boldsymbol{H} = \mu \boldsymbol{H}, \tag{7}$$

where $\mu = \mu_0(1+\chi)$ is the magnetic permeability and χ is the magnetic susceptibility. Note that we consider that the magnetic field $\boldsymbol{H}$ is small enough to assume the linear relationship between the magnetization and the magnetic field. In the absence of electric currents, $\boldsymbol{B}$ and $\boldsymbol{H}$ satisfy following magnetostatic Maxwell's equations [13,23],

$$\nabla \cdot \boldsymbol{B} = 0, \tag{8}$$

$$\nabla \times \boldsymbol{H} = 0. \tag{9}$$

Since a scalar potential ψ that satisfies

$$\boldsymbol{H} = -\nabla \psi \tag{10}$$

can be defined because $\boldsymbol{H}$ is a curl-free field, we obtain

$$\nabla \cdot (\mu \nabla \psi) = 0, \tag{11}$$

from Eqs. (7)–(10). The magnetic force $\boldsymbol{f_m}$ is now calculated [13,23,28] as

$$\boldsymbol{f_m} = \nabla \cdot \left\{ \mu \boldsymbol{H} \otimes \boldsymbol{H}^T - \frac{\mu}{2}(\boldsymbol{H} \cdot \boldsymbol{H})\boldsymbol{I} \right\}, \tag{12}$$

where $\boldsymbol{I}$ is the identity tensor.

3. Boundary condition

The no-slip boundary condition $\boldsymbol{u} = \boldsymbol{u_w}$ is applied to the two parallel walls: $\boldsymbol{u_w} = (\dot{\gamma} L_y/2, 0, 0)$ at the top wall and $\boldsymbol{u_w} = (-\dot{\gamma} L_y/2, 0, 0)$ at the bottom wall. As a boundary condition for the magnetic field, $\boldsymbol{H} = \boldsymbol{H_0}$ is given at both top and bottom walls. The periodic boundary conditions are applied in the x and z directions for both velocities and magnetic fields.

C. Numerical methods

To solve nearly incompressible multiphase flow, we employed the diffuse-interface lattice Boltzmann method [29]. The time evolution of the distribution function g for direction α is given as

$$g_\alpha(\boldsymbol{x} + \boldsymbol{c}_\alpha \Delta t, t + \Delta t) - g_\alpha(\boldsymbol{x}, t) = \Omega_\alpha + \Delta t \tilde{F}_\alpha, \tag{13}$$

$$\tilde{F}_\alpha = \omega_\alpha \left[1 + \frac{\boldsymbol{c}_\alpha \cdot \boldsymbol{u}}{c_s^2} + \frac{(\boldsymbol{c}_\alpha \cdot \boldsymbol{u})^2}{2c_s^4} - \frac{|\boldsymbol{u}|^2}{2c_s^2} \right] (\boldsymbol{c}_\alpha - \boldsymbol{u}) \cdot (\boldsymbol{f}_s + \boldsymbol{f}_m), \tag{14}$$

where $\boldsymbol{c}_\alpha$ is the discrete velocities, Ω_α is the collision operator, Δt is the discrete time, ω_α is the weight coefficient depending on the direction α, and c_s is the speed of sound. In this work, we use a multiple-relaxation time (MRT) model [30] for the stable computation, and the collision operator Ω in this model is given as

$$\Omega_\alpha = -(\mathcal{M}^{-1}\mathcal{S}\mathcal{M})_{\alpha\beta}\left[g_\beta(\boldsymbol{x}, t) - g_\beta^{\mathrm{eq}}(\boldsymbol{x}, t) \right], \tag{15}$$

where $\mathcal{M}$ is the transform matrix, $\mathcal{S}$ is the diagonal relaxation matrix, and g^{eq} is the equilibrium distribution function, which is given by

$$g_\alpha^{\mathrm{eq}} = p\omega_\alpha + \rho c_s^2 \omega_\alpha \left[\frac{\boldsymbol{c}_\alpha \cdot \boldsymbol{u}}{c_s^2} + \frac{(\boldsymbol{c}_\alpha \cdot \boldsymbol{u})^2}{2c_s^4} - \frac{|\boldsymbol{u}|^2}{2c_s^2} \right] - \frac{1}{2}\tilde{F}_\alpha. \tag{16}$$

Now the macroscopic variables are calculated as

$$\boldsymbol{u}(\boldsymbol{x}, t) = \frac{1}{\rho c_s^2} \sum_\alpha \boldsymbol{c}_\alpha g_\alpha(\boldsymbol{x}, t) + \frac{\Delta t}{2\rho}(\boldsymbol{f}_s + \boldsymbol{f}_m), \tag{17}$$

$$p(\boldsymbol{x}, t) = \sum_\alpha g_\alpha(\boldsymbol{x}, t). \tag{18}$$

In the lattice Boltzmann framework, the conservative phase-field equation [Eq. (3)] is discretized into

$$h_\alpha(\boldsymbol{x} + \boldsymbol{c}_\alpha \Delta t, t + \Delta t) - h_\alpha(\boldsymbol{x}, t) = -\frac{1}{\tau_\phi}\left[h_\alpha(\boldsymbol{x}, t) - h_\alpha^{\mathrm{eq}}(\boldsymbol{x}, t) \right], \tag{19}$$

where h_α is the phase-field distribution function and $\tau_\phi = 1/2 + M/(c_s^2 \Delta t)$ is the relaxation time. The equilibrium phase-field distribution function h_α^{eq} is given by

$$h_\alpha^{\mathrm{eq}} = \phi\omega_\alpha \left[1 + \frac{\boldsymbol{c}_\alpha \cdot \boldsymbol{u}}{c_s^2} + \frac{(\boldsymbol{c}_\alpha \cdot \boldsymbol{u})^2}{2c_s^4} - \frac{|\boldsymbol{u}|^2}{2c_s^2} \right] + \omega_\alpha \left(\tau_\phi - \frac{1}{2} \right) \Delta t \left[\frac{4\phi(1-\phi)}{\xi} \right] (\boldsymbol{c}_\alpha \cdot \boldsymbol{n}). \tag{20}$$

The phase function ϕ is calculated as

$$\phi(\boldsymbol{x}, t) = \sum_{\alpha} h_{\alpha}(\boldsymbol{x}, t). \tag{21}$$

The magnetic permeability μ at the interface is calculated by a linear interpolation based on the phase function ϕ as

$$\mu = \phi\mu_d + (1 - \phi)\mu_0. \tag{22}$$

It should be noted that the incompressible Navier-Stokes equation and phase-field equation are recovered from the lattice Boltzmann equations by applying the Chapman-Enskog expansion under small Mach number condition [31,32]. The diffuse-interface lattice Boltzmann method has been successfully applied to several multiphase flow problems [33–35].

We use the grid size $\Delta x = a/32$ and 12M computational grids to fully resolve the droplet motion inside the computational domain ($L_x \times L_y \times L_z = 7.5a \times 5.0a \times 10.0a$), and GPU parallelization (NVIDIA Tesla P100) is used to speed up the computation. Equations (10), (11), and (12) are dicretized with a second-order finite-difference scheme. The Poisson equation for the magnetic scalar potential is solved by using BiCG-stabilization method.

D. Dimensionless parameters

Our system can be characterized by three dimensionless parameters: Reynolds number (Re), capillary number (Ca), and Bond number (Bo),

$$\mathrm{Re} = \frac{\rho_0 \dot{\gamma} a^2}{\eta_0}, \tag{23}$$

$$\mathrm{Ca} = \frac{\eta_0 \dot{\gamma} a}{\sigma}, \tag{24}$$

$$\mathrm{Bo} = \frac{a\mu_0 H_0^2}{2\sigma}. \tag{25}$$

In this paper, Re is fixed to 0.1 while Ca and Bo are varied. Other dimensionless parameters are as follows: $\lambda = \eta_d/\eta_0 = 1$, $\rho_d/\rho_0 = 1$, and $\mu_d/\mu_0 = 2$.

III. RESULTS

In this section, we apply the magnetic field in three directions (x, y, and z directions), and report the droplet deformations and suspension rheologies. Our implementation is validated in the Appendix A. Figure 2 shows that the droplet deformation is drastically different by changing the external magnetic field, and the droplet shape is obtained by extracting the isosurface of the phase function $\phi = 0.5$. As is well known, the ferrofluid droplets elongate in the direction of the applied magnetic field. Figure 3 shows corresponding streamlines and the magnetic fields. As also reported in a previous work [21], the streamlines are less distorted when the magnetic field is in the x direction (velocity direction) and significantly distorted for the y direction (velocity gradient direction). When the magnetic field is applied to the z direction (vorticity direction), the cross-sectional area of the droplet at the shear plane becomes smaller compared to the other two directions and there is only partial distortion in the flow field. The magnetic fields have qualitative agreement with the previous 2D [13,22] and 3D [24] simulations.

A. Droplet deformation

Figure 4 shows the droplet deformation under three different directions of the external magnetic fields. In order to characterize the droplet deformation, we calculate the inertia tensor from the

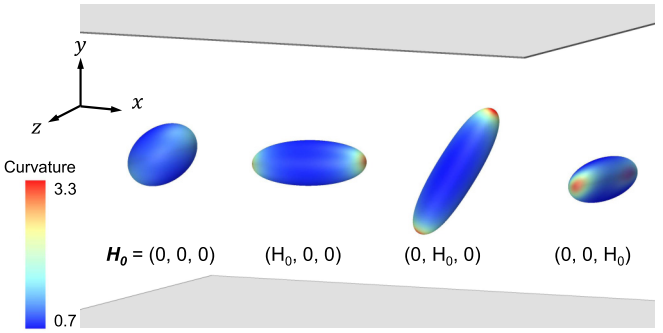

FIG. 2. Visualizations of the droplet deformation under different external magnetic field directions under the capillary number Ca = 0.15 and Bond numbers Bo = 8.0. The color of the droplet surface indicates the mean curvature of the surface shape.

droplet isosurface ($\phi = 0.5$) and fit the deformation into ellipsoidal shape [36] that has three principal lengths, ℓ_1, ℓ_2, and ℓ_3. Note that the droplet size is $\ell_1 = \ell_2 = \ell_3 = 2a$ at the initial resting state (Bo = 0 and Ca = 0), and Fig. 4 shows the deformation change $\Delta\ell_i/a = (\ell_i - 2a)/a$, where $i = 1, 2, 3$. In this figure, we assign two length ℓ_1 and ℓ_2 ($\ell_1 > \ell_2$) for deformations in the shear plane (x, y plane) and ℓ_3 for the z directional length as shown in Fig. 4(a).

Figures 4(b)–4(d) show that the droplet elongates in the direction that the external magnetic field is applied and shrinks in the two other directions. The qualitative tendency of the deformation has good agreement with the previous 2D simulations [13,21] and 3D theory and simulation (both under the magnetic field in y direction [24]) as shown in Appendix A. Note that we omitted the plots under

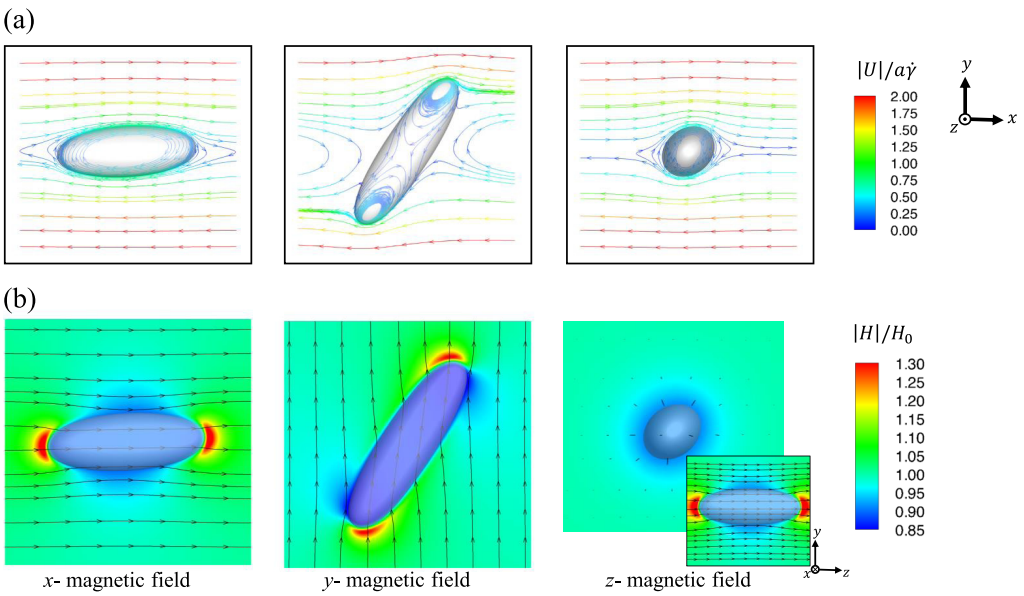

FIG. 3. (a) Streamlines and (b) magnetic fields under different external magnetic field directions under the capillary number Ca = 0.15 and Bond numbers Bo = 8.0. Both panels (a) and (b) show the cross section that includes the droplet center. Since the magnetic field is almost perpendicular to the (x, y) plane, the magnetic field in the (y, z) plane is also shown for z magnetic field.

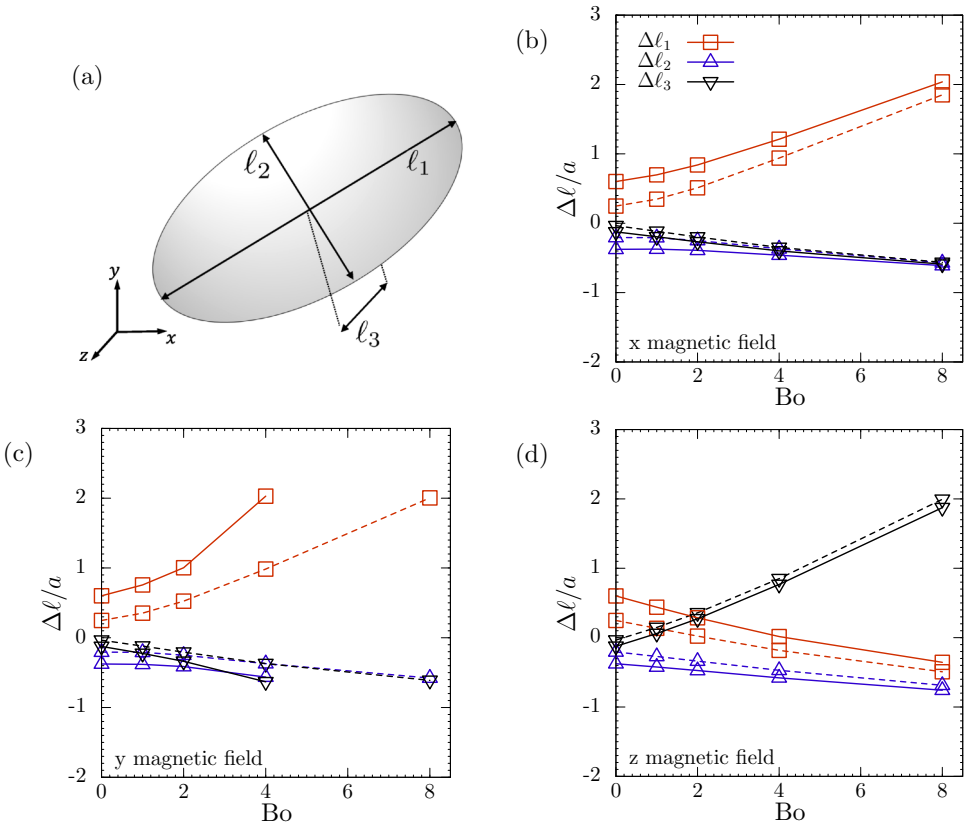

FIG. 4. (a) Schematic showing the definition of lengths ℓ_1, ℓ_2, and ℓ_3. [(b)–(d)] The droplet deformation $\Delta\ell_i = (\ell_i - 2a)/a$ $(i = 1, 2, 3)$ under the magnetic field in different directions: (b) x direction (velocity direction), (c) y direction (velocity gradient direction), and (d) z direction (vorticity direction). Dashed lines show $\Delta\ell$ under $\mathrm{Ca} = 0.1$ and solid lines are $\Delta\ell$ under $\mathrm{Ca} = 0.2$.

a high-magnetic-Bond-number condition in the y direction ($\mathrm{Bo} > 4$), because the droplet breaks up into several small droplets in these conditions [21,23], as also shown in Appendix B. Comparing the longest lengths $\Delta\ell$ of Figs. 4(b)–4(d) (i.e., $\Delta\ell_1$ for x and y external magnetic field and $\Delta\ell_3$ for z magnetic field) under $\mathrm{Ca} = 0.1$, which are shown with dashed lines, there are no drastic differences and they all reach $\Delta\ell/a \sim 2$ at $\mathrm{Bo} = 8$. The magnetic field direction has a small dependence on the deformation level because the Mason number, $\mathrm{Mn} = \mathrm{Ca}/\mathrm{Bo}$ [13,24,37,38], which characterizes the magnetic force compared to the applied shear, is small $\mathrm{Mn} \sim O(10^{-2})$ in this capillary number $\mathrm{Ca} = 0.1$. Although there are only small changes by increasing the capillary number to $\mathrm{Ca} = 0.2$, as shown in Figs. 4(b) and 4(d), deformation of the droplet under y magnetic field starts to deviate and it has steeper deformation change. The y magnetic field gives the largest deformation because the elongation in the y direction would result in elongation in the x direction as well, since the droplet experiences the large velocity difference.

We now term the direction that exhibits the longest length as a major axis, and the directions of two shorter lengths as minor axes. When there is no shear flow applied to the droplet ($\mathrm{Ca} = 0$), two minor axes of the droplet have same lengths and the droplet shape would be a prolate spheroid, which can be easily understood from the system axisymmetry [16,18]. Comparing the length of two minor axes appeared in Fig. 4, the droplet shapes are again prolate spheroids when the magnetic field is applied to the x and y directions: i.e., $\Delta\ell_2 \sim \Delta\ell_3$ for Figs. 4(b) and 4(c). On the other hand,

the droplets show nonaxisymmetric shapes ($\Delta\ell_1 \neq \Delta\ell_2$) when the magnetic field is applied to the z direction even up to Bo = 8. The difference between $\Delta\ell_1$ and $\Delta\ell_2$ becomes smaller with the Bo increase, and spheroidal shapes are expected by further increasing Bo. The droplet is not spheroidal only for the z direction (Bo < 8) because the magnetic field is not applied to the shear plane for this condition. Since the magnetic effect is dominant over the shear effect in our current setup [Mn $\sim$ O(10^{-2})], the shear flow has only minor effect on the droplet shape and the magnetic field tends to change the droplet shape from a nonspheroidal shape (Bo = 0) to a spheroidal shape. When the magnetic field is in the z direction, however, the shear effect is still present and the droplet keeps the nonspheroidal shape because this magnetic field has weaker effect on the droplet deformation in the shear plane.

B. Viscosity and normal stress difference

Next, we report how the suspension rheology is altered due to the external magnetic field. Since the Reynolds number in this system is small, stress due to the presence of droplets is evaluated using a particle stress tensor $\boldsymbol{\Sigma}^{(p)}$ [25,39,40]:

$$\boldsymbol{\Sigma}^{(p)} = \frac{1}{V}\boldsymbol{S} = \frac{1}{V}\int_A (\boldsymbol{x} \otimes \boldsymbol{q} + \eta(\lambda - 1)(\boldsymbol{u} \otimes \boldsymbol{n} + \boldsymbol{n} \otimes \boldsymbol{u}))dA, \tag{26}$$

where $V = L_x L_y L_z$ is the domain size, $\boldsymbol{S}$ is the stresslet, A is the droplet interface, and $\boldsymbol{q}$ is the load acting on the interface. The second term of the right-hand side of Eq. (26) vanishes for the current work because viscosity ratio is $\lambda = 1$ in this study. Notice that $\boldsymbol{q}$ corresponds to the stress jump $[\boldsymbol{\sigma}] \cdot \boldsymbol{n}$ across the interface, where $\boldsymbol{\sigma}$ is stress tensor and [ ] represents the jump condition. Since we use the diffuse interface model, $\boldsymbol{q}$ can be calculated as $\boldsymbol{q} = \int_h \boldsymbol{f} dh = \int_h (\boldsymbol{f}_s + \boldsymbol{f}_m) dh$, where h is a coordinate that is perpendicular to the fluid interface, and the stresslet can be rewritten as

$$\boldsymbol{S} = \int_A \int_h (\boldsymbol{x} \otimes \boldsymbol{f}) dh dA \approx \int_V (\boldsymbol{x} \otimes \boldsymbol{f}) dV. \tag{27}$$

Note we used in this conversion a fact that the body force $\boldsymbol{f}(\boldsymbol{x}) = \boldsymbol{0}$ if the position $\boldsymbol{x}$ is not at the droplet interface. The specific viscosity η_{sp} represents the increase in the suspension viscosity due to the particle shear stress [41,42] that is defined as

$$\eta_{\mathrm{sp}} = \frac{\Sigma^{(p)}_{yx}}{\eta_0 \dot{\gamma}}, \tag{28}$$

and Einstein [43] derived that the value is $\eta_{\mathrm{sp}} = 2.5\Phi$ for a dilute solution of a single sphere (radius a) with a volume fraction $\Phi = 4\pi a^3/(3V)$. In order to check the validity of the viscosity evaluation above, we also evaluate the viscosity in a different way: an evaluation based on the wall shear stress (WSS) [22]. The specific viscosity η_{sp} can also be calculated from the average shear stress at the wall as

$$\eta_{\mathrm{sp}}^{\mathrm{WSS}} = \frac{\frac{1}{W}\int_W \eta_0 \frac{\partial u_x}{\partial y} dW - \eta_0 \dot{\gamma}}{\eta_0 \dot{\gamma}}, \tag{29}$$

where W is the area of the wall and u_x is the x component of the velocity vector. Figures 5(a)–5(c) show the specific viscosity η_{sp} when the magnetic field is applied to three different directions, and two different evaluation of the viscosities η_{sp} and $\eta_{\mathrm{sp}}^{\mathrm{WSS}}$ have perfect agreements in all three directions. Modifying the system to 2D, we also evaluate the viscosity and compare the result with the previous 2D simulation [22]. Again, our simulation has quantitatively good agreement with the previous study.

Figure 5(d) summarizes the specific viscosity for different magnetic field directions and the capillary number. Note that the specific viscosity again has weak dependence of the capillary

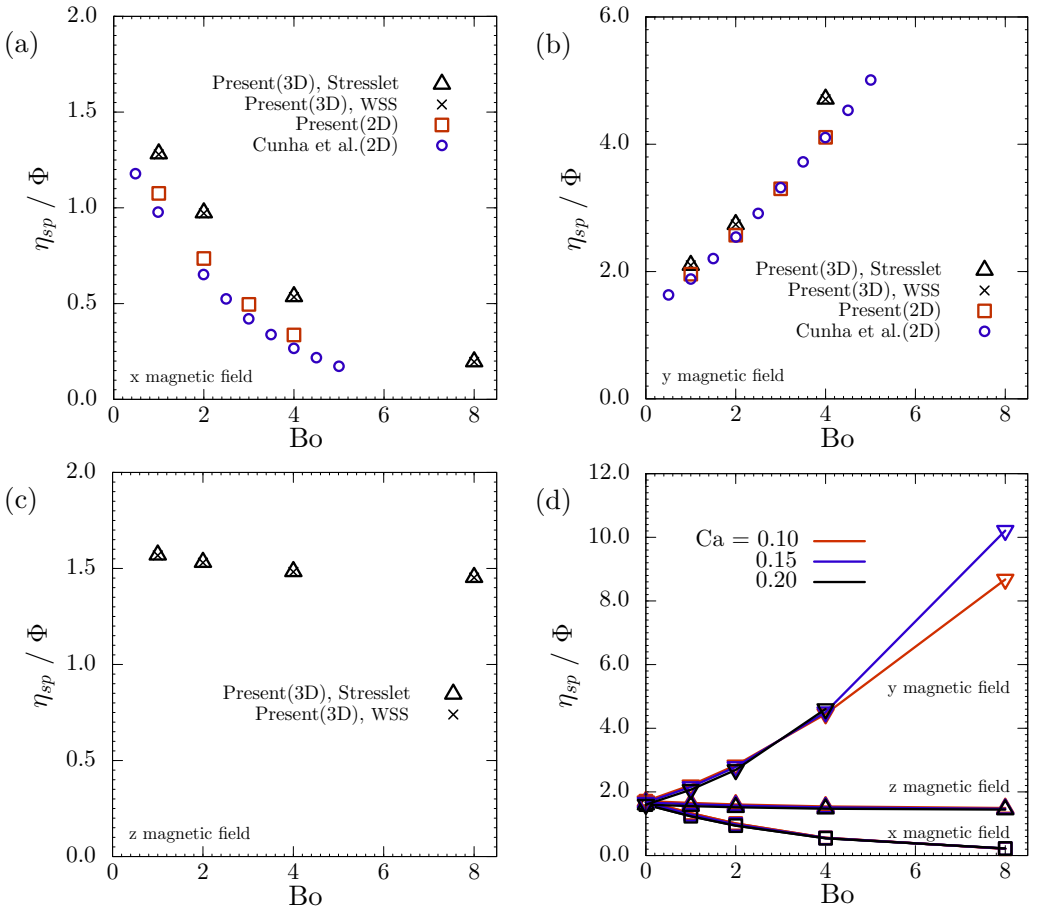

FIG. 5. The specific viscosity η_{sp} under (a) x, (b) y, and (c) z external magnetic field for Ca = 0.2. In (a) and (b), the results are compared with the previous 2D study reported by Cunha *et al.* [22]. (d) The specific viscosity η_{sp} of the droplet suspension under three different external magnetic directions.

number, because the conditions are in the Bond number dominant regime, Mn $\ll 1$. The viscosity decreases with the Bond number when the magnetic field is applied to the x direction, while it increases for the y direction, and these tendencies agree well with the previous reports in 2D simulations [21,22]. At large Bond number, Bo = 8, the viscosity becomes 620% or 12% compared to the viscosity at Bo = 0 when the magnetic field is applied to the y and x directions, respectively.

From the flow field shown in Fig. 3(a), the small viscosity η_{sp} is expected when the magnetic field is in the z direction since there is less flow disturbance. Surprisingly, the viscosity slightly decreases with the Bond number and its change is not as drastic as in the other two directions when the magnetic field is in this direction. In order to reveal the viscosity difference in two magnetic field directions, the x and z directions, we now show the orientation angle of the droplet in the shear plane θ_d in Fig. 6. Note that the angle is evaluated from the eigenvectors of the inertia tensor, which was also used to fit the droplet shape into ellipsoidal shape in the previous section. The orientation angle $\theta_d = \arctan(v_y/v_x)$ is evaluated from an eigenvector (v_x, v_y, v_z) that has the largest eigenvalue in the shear plane. As shown in Fig. 6(a), the angle increases [y direction; also Fig. 6(c)] or decreases [x direction; Fig. 6(b)] when the magnetic field is applied to the shear plane, while the

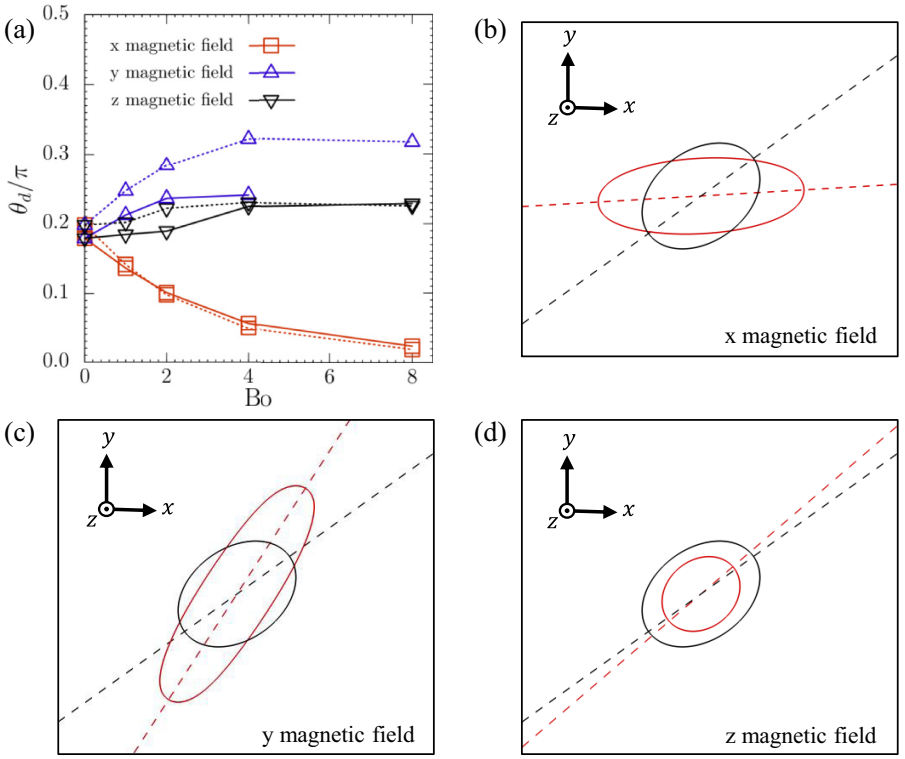

FIG. 6. (a) The orientation angle of the droplet θ_d. The solid lines show θ_d under Ca = 0.2 and the dotted lines show Ca = 0.15. [(b)–(d)] The black solid lines show the cross sectional shape of the droplet under no magnetic field (Bo = 0 and Ca = 0.15), while the red solid lines show the shape under the magnetic field (Bo = 8.0 and Ca = 0.15) in three different directions. Dashed lines show the corresponding orientation angles.

angle stays relatively the same $\theta_d = 0.20\pi - 0.25\pi$ for the z direction [Fig. 6(d)]. This difference in the orientation angle is directly connected to the difference in the viscosity $\eta_{\rm sp}$. When there is no external force applied to the particle, such as the pure droplet or capsule suspensions, we showed in our previous study [41] that the shear component of the stresslet S_{yx} can be rewritten as

$$S_{yx} = (S_1 - S_2)\sin 2\theta_s \tag{30}$$

when the particle is ellipsoidal, where S_1 and S_2 ($S_1 > S_2$) are the eigenvalues of the stresslet in the shear plane and θ_s is the orientation angle of the stresslet obtained from the eigenvector of S_1. Note that two orientation angles become the same $\theta_d = \theta_s$ when the droplet is a perfect ellipsoidal shape. From Eq. (30), the viscosity $\eta_{\rm sp}$ would reach maximum when the angle is $\theta_s = \theta_d = \pi/4$. Although the particle is not torque free in the present study, this discussion can be extended and utilized to understand the viscosity $\eta_{\rm sp}$ difference in Fig. 5(d). When the magnetic field is applied to the flow direction (x direction), the viscosity decreased because the orientation angle θ_d decreased and the principal directions of the stress $\mathbf{\Sigma}^p$ (symmetric component) become closer to the x and y axes. When the magnetic field is applied to the vorticity direction (z direction), on the other hand, the orientation angle is still facing $\theta_d \sim \pi/4$ even for high-Bond-number conditions, and as a result, the visocsity stays relatively the same. The orientation angle θ_d has weak dependence on the Bond number for this case because the magnetic field is not applied to the shear plane. This angle difference resulted in the viscosity difference shown in Fig. 5(d).

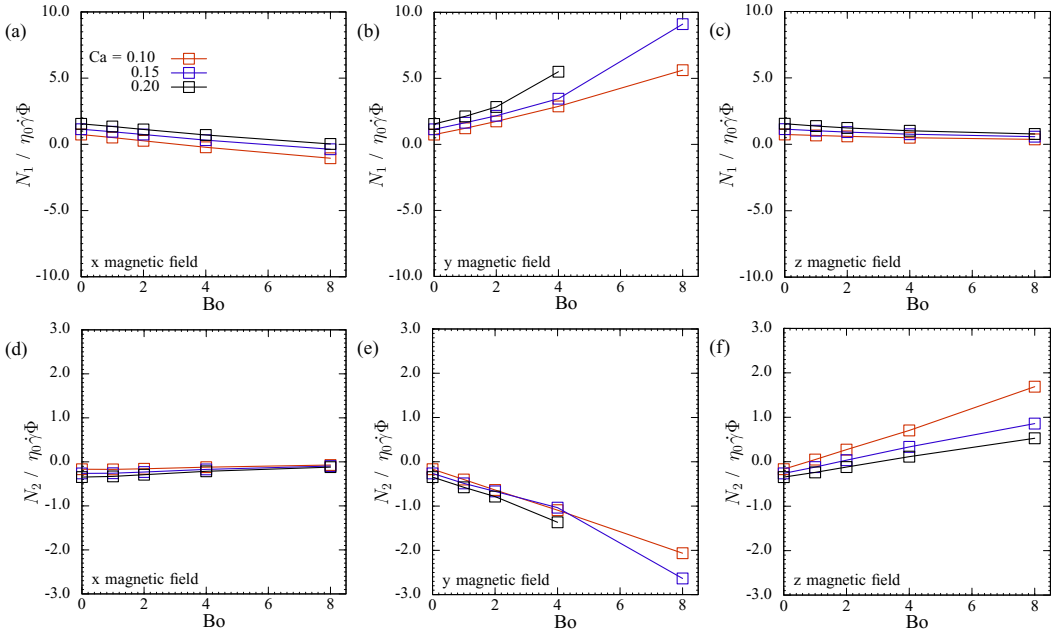

FIG. 7. [(a)–(c)] The first normal stress difference N_1 under different directions of the external magnetic field (a) x, (b) y, and (c) z directions. [(d)–(f)] The second normal stress difference N_2 under three directions of the external magnetic field, the x, y, and z directions, respectively.

Finally, we evaluate the first N_1 and second N_2 normal stress differences defined as

$$\frac{N_1}{\eta\dot{\gamma}\Phi} = \frac{\Sigma_{xx}^{(p)} - \Sigma_{yy}^{(p)}}{\eta\dot{\gamma}\Phi}, \tag{31}$$

$$\frac{N_2}{\eta\dot{\gamma}\Phi} = \frac{\Sigma_{yy}^{(p)} - \Sigma_{zz}^{(p)}}{\eta\dot{\gamma}\Phi}. \tag{32}$$

When the droplet deforms under the shear flow but under no external field (Bo = 0) and Re $\ll 1$, the droplet tries to shrink in the velocity direction (x direction; $S_{xx} > 0$) and to expand in the two other directions (y and z directions; $S_{yy} < S_{zz} < 0$). Therefore, the first normal stress difference is positive while the second normal stress difference is negative for a droplet suspension under Bo = 0 [25,44–47], and we confirmed that our numerical results satisfy these relations, $N_1 > 0$ and $N_2 < 0$.

Figure 7 shows the normal stress differences under three different directions of the magnetic field, and it indicates that values N_1 and N_2 can be controlled by imposing the external magnetic field to the relevant direction. When the magnetic field is applied to the ith direction, the stresslet component S_{ii} decreases because the droplet expands and elongates in this direction due to the magnetic force $\boldsymbol{f}_m$. Using this character, N_1 increases (decreases) when the magnetic field is applied to the y direction (x direction) and N_2 increases (decreases) when the magnetic field is applied to the z direction (y direction). The quantitative tendency of N_1 has good agreement with recent publication using 2D simulation [22]. Interestingly, even the sign of normal stress differences can be changed by imposing the external field. By imposing magnetic fields in the x direction and the z direction under high-Bond-number conditions, N_1 becomes negative and N_2 becomes positive, respectively, which are opposite from the normal droplet suspensions [25]. Previous papers [45,47] reported that the same sign reversals of the normal stress differences, $N_1 < 0$ and $N_2 > 0$, occur for the droplet suspension when the Reynolds number is high, Re $\sim O(1)$. Our current results show that

the ferrofluid droplets are practical material to change the sign of the normal stress differences even under small-Reynolds-numbers Re $< O(10^{-1})$.

In summary, we can conclude from our simulation that the ferrofluid droplet can be a practical tool controlling the rheological properties of the suspension.

IV. CONCLUSION

In this paper, we reported the rheology of a dilute ferrofluid droplet suspension under simple shear flow using the 3D lattice-Boltzmann simulation and the phase-field model. In our simulation, we utilize 12M computational grids to fully resolve the droplet deformation, and GPU parallelization is used to speed up the computation. The droplet deforms due to the background shear flow, and its shape can be altered by imposing the external magnetic field. By changing the external field strength and direction, we found that the suspension rheologies are drastically different. The viscosity increase (decrease) with the external field when the external field is applied to the velocity gradient direction (velocity direction). Note that we call the x, y, and z directions the velocity direction, velocity gradient direction, and vorticity direction, respectively. Just by imposing the external magnetic field, the specific viscosity becomes $12 \sim 620\%$ compared to the condition under no external field. The magnetic force is also practical to control the normal stresses, since the stresslet S_{ii} decreases when the magnetic field is applied to the ith direction. In order to increase (decrease) the first normal stress difference N_1, the external magnetic field should be applied to the velocity gradient direction (velocity direction). To increase (decrease) the second normal stress difference N_2, the external magnetic field should be applied to the vorticity direction (velocity gradient direction). By applying the magnetic field, we also show that the normal stresses N_1, N_2 even show opposite sign from the normal droplet solutions ($N_1 > 0, N_2 < 0$).

The major advance of this work was to report the rheological properties that can be only revealed under 3D system, such as the normal stress difference N_2 and the suspension rheology under z directional magnetic field, with the help of parallelized large-scale lattice Boltzmann method (LBM) simulations. Our results suggest that the ferrofluid droplet can be a practical material to control the suspension rheology by imposing the magnetic field. We believe that our findings would be an essential building block for the future findings in the ferrofluid suspensions.

ACKNOWLEDGMENTS

This work was supported by JSPS (Japan Society for the Promotion of Science) KAKENHI Grants No. 20K14649 and No. 19K20672 and JST (Japan Science and Technology Agency) ACT-X Grant No. JPMJAX190S Japan and Multidisciplinary Research Laboratory System for Future Developments (MIRAI LAB).

S.I. and D.M. contributed equally to this work.

APPENDIX A: BENCHMARK

In this section, we validate our simulation result with three different benchmarks. Note again that we fixed the following conditions: the domain size $L_x \times L_y \times L_z = 7.5a \times 5.0a \times 10.0a$, grid size $\Delta x = a/32$, Reynolds number Re $= 0.1$, density ratio $\rho_d/\rho_0 = 1$, viscosity ratio $\eta_d/\eta_0 = \lambda = 1$, and permeability ratio $\mu_d/\mu_0 = 2$ (i.e., magnetic susceptibility of the droplet $\chi = 1$).

1. Dilute droplet suspensions under simple shear flow

First, we validate the droplet deformation and the suspension rheology under simple shear flow but with no magnetic field Bo $= 0$. At small deformation limit, Taylor [49,50] predicted that the Taylor deformation parameter D would converge to

$$D = \frac{19\lambda + 16}{16\lambda + 16}\mathrm{Ca}, \tag{A1}$$

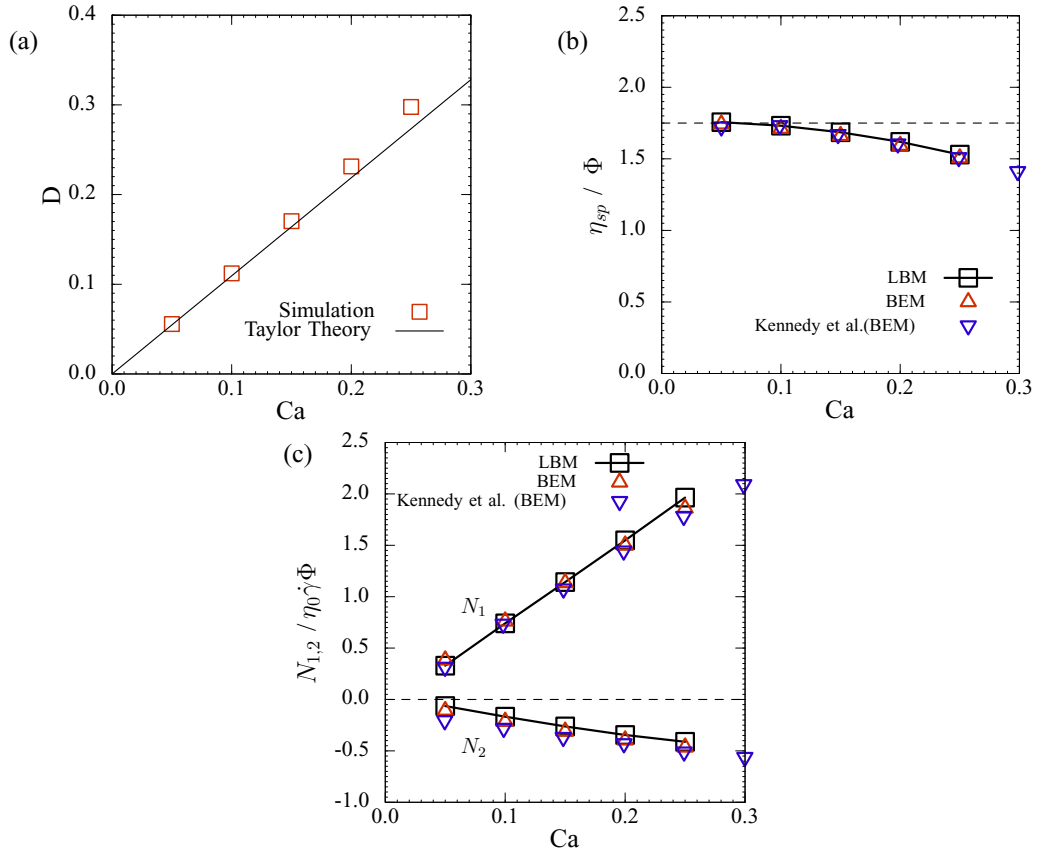

FIG. 8. (a) Droplet deformation (Taylor parameter, D) under simple shear flow. The solid line shows the Taylor's prediction (A1). (b) The specific viscosity $\eta_{\rm sp}$ under simple shear flow. Dashed line is the Taylor's prediction $\eta_{\rm sp} = 1.75\Phi$. The result of our present simulation (LBM) is compared with our BEM simulation [48] and another previous work [44]. (c) The first and second normal stress differences under simple shear flow.

where λ is the viscosity ratio. Note that the estimation is valid under negligible Reynolds number $\mathrm{Re} \ll 1$ and with no walls ($L_y \to \infty$) or walls with large separate distance $L_y/a \geqslant 5$ [51]. Figure 8(a) shows that our result has good agreement with the prediction. The deformation starts to deviate from the estimation because the estimation only stands under small deformation limit $\mathrm{Ca} \ll 1$.

Taylor [52] also predicted that the specific viscosity of a dilute droplet solution is

$$\eta_{\rm sp} = 2.5\Phi\frac{\eta_d + 2\eta_0/5}{\eta_d + \eta_0} = 2.5\Phi\frac{\lambda + 2/5}{\lambda + 1} \tag{A2}$$

under the small deformation limit ($\mathrm{Ca} \to 0$) where Φ is the volume fraction of the droplet. Figure 8(b) shows the specific viscosity and Fig. 8(c) the normal stress differences of the droplet solution under no external magnetic field from our simulations. Note that the stress due to the particle is evaluated by the particle stress tensor (26). The obtained $\eta_{\rm sp}$ curve converges to the Taylor's prediction $\eta_{\rm sp} = 1.75\Phi$ ($\lambda = 1$) by decreasing the capillary number. Both the viscosity and normal stress differences have good agreement with our simulation based on the boundary element method (BEM) [48] and a previous numerical study [44].

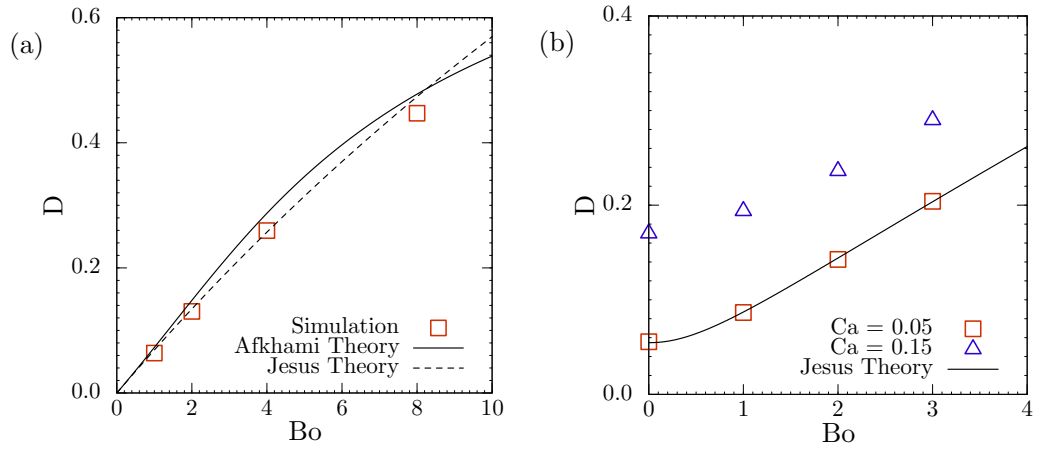

FIG. 9. (a) Droplet deformation under the external magnetic field. The solid line shows a prediction from a previous study (A3), while the dashed line shows the other prediction (A6). (b) Droplet deformation under both simple shear flow and external magnetic field. The solid lines show a prediction from a previous study (A6).

2. Droplet deformation under the external magnetic field

Second, we validate the droplet deformation under an external magnetic field but with no shear flow $\mathrm{Ca} = 0$. Assuming an axisymmetric shape, Afkhami *et al.* [16] analytically estimated the droplet deformation, and the prediction has been used to validate the simulation result in previous studies [13,24]. Thanks to their equation, the Taylor parameter D and the Bond number Bo satisfy the following relation:

$$\mathrm{Bo} = \left(\frac{1}{\chi} + k\right)^2 \left(\frac{1+D}{1-D}\right)^{1/3} \left\{2\left(\frac{1+D}{1-D}\right) - \left(\frac{1+D}{1-D}\right)^{-2} + 1\right\}, \tag{A3}$$

where

$$k = \frac{1-E^2}{2E^3}\left(\ln\frac{1+E}{1-E} - 2E\right), \tag{A4}$$

$$E = \sqrt{1 - \left(\frac{1+D}{1-D}\right)^2}. \tag{A5}$$

Our deformation shown in Fig. 9(a) has good agreement with the estimation. Note that we also compared the deformation with the other theory [24], which is explained in detail in the next subsection.

3. Droplet deformation under both simple shear and external magnetic field

Finally, we validate the droplet deformation under presence of both the external magnetic field and shear flow: $\mathrm{Bo} \neq 0$ and $\mathrm{Ca} \neq 0$. Jesus *et al.* [24] derived the droplet deformation with an asymptotic theory with assumptions, $\mathrm{Ca} \ll 1$ and $\mathrm{Bo} \ll 1$. When the magnetic field in the velocity gradient direction (y direction), the Taylor parameter is given as a function of the capillary number and Bond number as

$$D \approx \frac{\sqrt{\alpha^2 \mathrm{Ca}^2 + \beta^2 \mathrm{Bo}^2}}{2 + \beta \mathrm{Bo}/3}, \tag{A6}$$

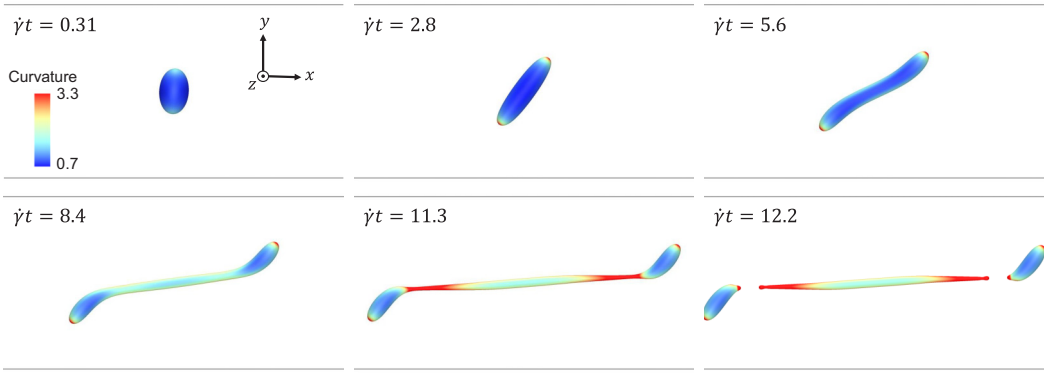

FIG. 10. Deformation and breakup of the droplet under Ca = 0.2 and Bo = 8.0. Magnetic field is applied to the y direction.

where

$$\alpha = \frac{19\lambda + 16}{8(\lambda + 1)}, \tag{A7}$$

$$\beta = \frac{3\chi(2\chi + 1)}{4(\chi + 3)^2}. \tag{A8}$$

Although our simulation result has good agreement with the theory at small capillary number Ca = 0.05 as shown in Fig. 9(b), there are deviations for high capillary number, Ca = 0.15, because the condition is outside the range of the small deformation limit Ca $\ll$ 1.

APPENDIX B: BREAKUP OF DROPLET UNDER A HIGH-MAGNETIC-BOND-NUMBER CONDITION

In this Appendix, we show in Fig. 10 that the droplet breaks up into small droplets when the magnetic field is applied to the y direction (velocity gradient direction) under a high-Bond-number condition (Bo = 8.0). The domain size $L_x \times L_y \times L_z = 20.5a \times 3.2a \times 10.0a$ and 21M computational grid is used. As also reported in the previous works [21,23] the droplet first elongates in the flow direction (x direction) and exhibits an S shape. Because the droplet neck becomes thinner, it eventually breaks up into three small droplets.

[1] K. E. Peyer, L. Zhang, and B. J. Nelson, Bio-inspired magnetic swimming microrobots for biomedical applications, Nanoscale **5**, 1259 (2013).
[2] R. M. Erb, J. J. Martin, R. Soheilian, C. Pan, and J. R. Barber, Actuating soft matter with magnetic torque, Adv. Funct. Mater. **26**, 3859 (2016).
[3] F. Y. Ogrin, P. G. Petrov, and C. P. Winlove, Ferromagnetic Microswimmers, Phys. Rev. Lett. **100**, 218102 (2008).
[4] L. Zhang, J. J. Abbott, L. Dong, K. E. Peyer, B. E. Kratochvil, H. Zhang, C. Bergeles, and B. J. Nelson, Characterizing the swimming properties of artificial bacterial flagella, Nano Lett. **9**, 3663 (2009).
[5] J. K. Hamilton, A. D. Gilbert, P. G. Petrov, and F. Y. Ogrin, Torque driven ferromagnetic swimmers, Phys. Fluids **30**, 092001 (2018).
[6] F. Meng, D. Matsunaga, J. M. Yeomans, and R. Golestanian, Magnetically-actuated artificial cilium: A simple theoretical model, Soft Matter **15**, 3864 (2019).

[7] D. Matsunaga, J. K. Hamilton, F. Meng, N. Bukin, E. L. Martin, F. Y. Ogrin, J. M. Yeomans, and R. Golestanian, Controlling collective rotational patterns of magnetic rotors, Nat. Commun. **10**, 1 (2019).
[8] T. Kawai, D. Matsunaga, F. Meng, J. Yeomans, and R. Golestanian, Degenerate states, emergent dynamics and fluid mixing by magnetic rotors, Soft Matter **16**, 6484 (2020).
[9] R. Zhou, F. Bai, and C. Wang, Magnetic separation of microparticles by shape, Lab Chip **17**, 401 (2017).
[10] R. Zhou, C. A. Sobecki, J. Zhang, Y. Zhang, and C. Wang, Magnetic Control of Lateral Migration of Ellipsoidal Microparticles in Microscale Flows, Phys. Rev. Appl. **8**, 024019 (2017).
[11] D. Matsunaga, F. Meng, A. Zöttl, R. Golestanian, and J. M. Yeomans, Focusing and Sorting of Ellipsoidal Magnetic Particles in Microchannels, Phys. Rev. Lett. **119**, 198002 (2017).
[12] D. Matsunaga, A. Zöttl, F. Meng, R. Golestanian, and J. M. Yeomans, Far-field theory for trajectories of magnetic ellipsoids in rectangular and circular channels, IMA J. Appl. Math. **83**, 767 (2018).
[13] M. R. Hassan, J. Zhang, and C. Wang, Deformation of a ferrofluid droplet in simple shear flows under uniform magnetic fields, Phys. Fluids **30**, 092002 (2018).
[14] J. Zhang, M. R. Hassan, B. Rallabandi, and C. Wang, Migration of ferrofluid droplets in shear flow under a uniform magnetic field, Soft Matter **15**, 2439 (2019).
[15] S. Banerjee, M. Fasnacht, S. Garoff, and M. Widom, Elongation of confined ferrofluid droplets under applied fields, Phys. Rev. E **60**, 4272 (1999).
[16] S. Afkhami, A. Tyler, Y. Renardy, M. Renardy, T. S. Pierre, R. Woodward, and J. S. Riffle, Deformation of a hydrophobic ferrofluid droplet suspended in a viscous medium under uniform magnetic fields, J. Fluid Mech. **663**, 358 (2010).
[17] G.-P. Zhu, N.-T. Nguyen, R. V. Ramanujan, and X.-Y. Huang, Nonlinear deformation of a ferrofluid droplet in a uniform magnetic field, Langmuir **27**, 14834 (2011).
[18] A. Ghaffari, S. H. Hashemabadi, and M. Bazmi, Cfd simulation of equilibrium shape and coalescence of ferrofluid droplets subjected to uniform magnetic field, Colloids Surf. A **481**, 186 (2015).
[19] I. Torres-Díaz and C. Rinaldi, Recent progress in ferrofluids research: Novel applications of magnetically controllable and tunable fluids, Soft Matter **10**, 8584 (2014).
[20] J. R. Smart and D. T. Leighton, Jr., Measurement of the drift of a droplet due to the presence of a plane, Phys. Fluids A: Fluid Dynam. **3**, 21 (1991).
[21] L. H. Cunha, I. R. Siqueira, T. F. Oliveira, and H. D. Ceniceros, Field-induced control of ferrofluid emulsion rheology and droplet break-up in shear flows, Phys. Fluids **30**, 122110 (2018).
[22] L. Cunha, I. Siqueira, F. Cunha, and T. Oliveira, Effects of external magnetic fields on the rheology and magnetization of dilute emulsions of ferrofluid droplets in shear flows, Phys. Fluids **32**, 073306 (2020).
[23] M. R. Hassan and C. Wang, Magnetic field induced ferrofluid droplet breakup in a simple shear flow at a low reynolds number, Phys. Fluids **31**, 127104 (2019).
[24] W. C. Jesus, A. M. Roma, and H. D. Ceniceros, Deformation of a sheared magnetic droplet in a viscous fluid, Commun. Comput. Phys **24**, 332 (2017).
[25] M. Loewenberg and E. Hinch, Numerical simulation of a concentrated emulsion in shear flow, J. Fluid Mech. **321**, 395 (1996).
[26] P.-H. Chiu and Y.-T. Lin, A conservative phase field method for solving incompressible two-phase flows, J. Comput. Phys. **230**, 185 (2011).
[27] J. U. Brackbill, D. B. Kothe, and C. Zemach, A continuum method for modeling surface tension, J. Comput. Phys. **100**, 335 (1992).
[28] R. E. Rosensweig, *Ferrohydrodynamics* (Cambridge University Press, Cambridge, UK, 1985).
[29] A. Fakhari and D. Bolster, Diffuse interface modeling of three-phase contact line dynamics on curved boundaries: A lattice boltzmann model for large density and viscosity ratios, J. Comput. Phys. **334**, 620 (2017).
[30] D. d'Humieres, Multiple–relaxation–time lattice boltzmann models in three dimensions, Philos. Trans. Roy. Soc. Lond.. Ser. A: Math. Phys. Eng. Sci. **360**, 437 (2002).
[31] S. Chen and G. D. Doolen, Lattice boltzmann method for fluid flows, Annu. Rev. Fluid Mech. **30**, 329 (1998).
[32] T. Krüger, H. Kusumaatmaja, A. Kuzmin, O. Shardt, G. Silva, and E. M. Viggen, *The Lattice Boltzmann Method*, Vol. 10 (Springer International Publishing, Cham, 2017), 4.

[33] H. Wang, X. Yuan, H. Liang, Z. Chai, and B. Shi, A brief review of the phase-field-based lattice boltzmann method for multiphase flows, Capillarity **2**, 33 (2019).
[34] N. Takada, J. Matsumoto, S. Matsumoto, and K. Kurihara, Phase-field model-based simulation of two-phase fluid motion on partially wetted and textured solid surface, J. Comput. Sci. **17**, 315 (2016).
[35] J. Ohta, S. Ishida, T. Kawase, Y. Katori, and Y. Imai, A computational fluid dynamics simulation of liquid swallowing by impaired pharyngeal motion: Bolus pathway and pharyngeal residue, Am. J. Physiol. Gastrointest. Liver Physiol. **317**, G784 (2019).
[36] E. Lac, D. Barthes-Biesel, N. Pelekasis, and J. Tsamopoulos, Spherical capsules in three-dimensional unbounded stokes flows: Effect of the membrane constitutive law and onset of buckling, J. Fluid Mech. **516**, 303 (2004).
[37] S. Melle, O. G. Calderón, M. A. Rubio, and G. G. Fuller, Microstructure evolution in magnetorheological suspensions governed by mason number, Phys. Rev. E **68**, 041503 (2003).
[38] M. Driscoll, B. Delmotte, M. Youssef, S. Sacanna, A. Donev, and P. Chaikin, Unstable fronts and motile structures formed by microrollers, Nat. Phys. **13**, 375 (2017).
[39] G. Batchelor, The stress system in a suspension of force-free particles, J. Fluid Mech. **41**, 545 (1970).
[40] J. Bławzdziewicz, P. Vlahovska, and M. Loewenberg, Rheology of a dilute emulsion of surfactant-covered spherical drops, Physica A **276**, 50 (2000).
[41] D. Matsunaga, Y. Imai, T. Yamaguchi, and T. Ishikawa, Rheology of a dense suspension of spherical capsules under simple shear flow, J. Fluid Mech. **786**, 110 (2016).
[42] H. Ito, D. Matsunaga, and Y. Imai, Shear viscosity of bimodal capsule suspensions in simple shear flow, Phys. Rev. Fluids **4**, 113601 (2019).
[43] A. Einstein, Eine neue bestimmung der moleküldimensionen, Ann. Phys. **324**, 289 (1906).
[44] M. R. Kennedy, C. Pozrikidis, and R. Skalak, Motion and deformation of liquid drops, and the rheology of dilute emulsions in simple shear flow, Comput. Fluids **23**, 251 (1994).
[45] X. Li and K. Sarkar, Effects of inertia on the rheology of a dilute emulsion of drops in shear, J. Rheol. **49**, 1377 (2005).
[46] D. Pan, N. Phan-Thien, and B. C. Khoo, Dissipative particle dynamics simulation of droplet suspension in shear flow at low capillary number, J. Non-Newt. Fluid Mech. **212**, 63 (2014).
[47] P. Srivastava, A. R. Malipeddi, and K. Sarkar, Steady shear rheology of a viscous emulsion in the presence of finite inertia at moderate volume fractions: Sign reversal of normal stress differences, J. Fluid Mech. **805**, 494 (2016).
[48] D. Matsunaga, Y. Imai, C. Wagner, and T. Ishikawa, Reorientation of a single red blood cell during sedimentation, J. Fluid Mech. **806**, 102 (2016).
[49] G. I. Taylor, The formation of emulsions in definable fields of flow, Proc. Roy. Soc. Lond. Ser. A **146**, 501 (1934).
[50] R. G. Larson, *The Structure and Rheology of Complex Fluids*, Vol. 150 (Oxford University Press, New York, 1999).
[51] N. Ioannou, H. Liu, and Y. Zhang, Droplet dynamics in confinement, J. Comput. Sci. **17**, 463 (2016).
[52] G. I. Taylor, The viscosity of a fluid containing small drops of another fluid, Proc. Roy. Soc. Lond. Ser. A **138**, 41 (1932).